Modelling Chloride Transport in Alkali-Activated Slags

Shishir Mundra[1,2], Dale P. Prentice[1,3], Susan A. Bernal[1,4], John L. Provis[1*]

[1] Department of Materials Science and Engineering, The University of Sheffield, Sir Robert Hadfield Building, Sheffield, S1 3JD, United Kingdom

[2] Division 7.4, Technology of Construction Materials, Bundesanstalt für Materialforschung und -prüfung (BAM), Unter den Eichen 87, Berlin 12205, Germany

[3] Civil and Environmental Engineering Department, University of California, Los Angeles, CA 90095, United States of America

[4] School of Civil Engineering, University of Leeds, Woodhouse Lane, Leeds, LS2 9JT, United Kingdom

[*]Corresponding author: j.provis@sheffield.ac.uk

Abstract

The service-life of steel-reinforced concrete structures is primarily determined by the ability of the concrete cover to resist chloride ingress. With limited literature available on the ingress of chloride into alkali-activated slags (AAS) under service conditions, it is critical that this is described by appropriate models. This paper describes an interactive software framework to relate chloride ingress into AAS with the chemistry of the concrete cover, by considering the chloride binding capacity and porosity of the binder as a function of time, based on thermodynamic calculations of the phase assemblage as a function of slag and activator composition. This provides a major step towards developing the ability to predict the ingress of chlorides in alkali-activated concretes from a sound theoretical basis, which is essential in providing confidence in the durability of these materials in essential infrastructure applications.

Keywords: Thermodynamic Calculations (B); Diffusion (C); Chloride (D); Alkali Activated Cement (D); Durability (C).

1 Introduction

The service life of steel reinforced concrete structures in the presence of chlorides is often described by the classical model proposed by Tuutti [1]. The model can be broadly categorised into the transport process *(initiation phase)*, the breakdown of steel passivity *(onset of corrosion)*, and the time between the onset of corrosion and the end of serviceability *(propagation phase)*. The duration of the initiation phase is primarily a function of the chemistry of the hydration products forming in the binder and their ability to bind chloride ions, the pore structure of the cement matrix, the pore solution chemistry and its ionic strength [2], while the onset of corrosion is governed by the local characteristics of the steel-concrete interface (SCI) – pore solution chemistry and its pH, the chloride concentration and the chemical composition of the steel surface [3,4]. The duration of the propagation phase is determined by the ability of the SCI to sustain stable pit growth and a reduction in the cross section of the steel reinforcement [3,4].

In the case of Portland cement (PC) based steel-reinforced concretes, a significant amount of research has been carried out to gain an understanding of the initiation phase, the onset of corrosion and the propagation phase. However, some critical questions regarding the onset of corrosion in PC based systems remain unanswered, particularly those pertaining to the influence of the SCI [3].

Alkali-activated slag (AAS) binders are less well understood than PC, and there remains a significant need to improve the understanding of the long-term performance of AAS when used in steel-reinforced concrete structures, as field data spanning decades or more are very limited. The initiation phase, or the time taken for chloride ingress through the cover of AAS concretes, has been observed in some instances to be notably longer than in PC based systems, and this has been attributed to denser microstructures, higher chloride binding capacity, and/or higher ionic strength of the pore solutions in AAS [5–7], but remains incompletely understood. The extent of chloride binding in AAS has been found to depend on the chemical composition of slag used, the phase assemblage evolution formed upon activation, and the alkalinity of the resulting pore solution [8]. The pore solution of AAS is highly reducing due to the presence of reduced sulfur species supplied by the slag, which at high concentrations has also been observed to alter both the passivation capability and the surface chemistry of the steel reinforcement [9] from those encountered in PC based concretes. The breakdown of passivity and the subsequent propagation of steel corrosion in concrete structures has been associated with the concept of a chloride ‘threshold’ value [10], but as is the case for PC, the available data on the chloride ‘threshold’ value for AAS are very scattered.

The various parameters that control the initiation, onset of corrosion and propagation phases are highly convoluted and inter-dependent. Therefore, any predictive service life model needs to consider the influence of the concrete cover characteristics on the transport processes, as well as the conditions prevailing at the SCI for corrosion to initiate and propagate. This study provides an underpinning framework focused on the first of these two points, by coupling thermodynamic simulations predicting the chemistry of the concrete cover with numerical modelling of chloride diffusion and binding.

2 Developing a modelling framework

A framework for predicting chloride ingress into AAS based concretes was developed in the MATLAB software environment. The MATLAB script, which is provided as Supporting Information accompanying this paper, incorporates the thermodynamic data generated for various chemistries of commercial blast furnace slags and activators (discussed in detail in Section 2.1), the transport and chloride binding properties of AAS (discussed in detail in Section 2.2) and then calculates the chloride profiles for a specified AAS concrete for the first 70 years. The script works from input data provided by the user regarding the composition of the slag and the activator of interest, concentration of the chloride exposure solution, and the concrete cover depth. To investigate the application of the proposed model, several slag compositions were selected from the literature [7,11] and are shown in Table 1.

Table 1: The chemical compositions of various slags considered in this study, expressed as wt. % of oxides in this table regardless of the true oxidation state of each element. Data for M01, M05, M06, and M14 are from [7], and those for M08, M11, and M13 are from [11].

	M01	**M05**	**M06**	**M08**	**M11**	**M13**	**M14**
CaO	42.9	42.3	41.3	35.8	34.6	33.4	33.9
SiO_2	31.6	32.3	36.0	38.2	37.1	36.4	37.4
Al_2O_3	14.6	13.3	11.3	12	11.5	11.3	9.0
Fe_2O_3	1.1	0.6	0.3	1.6	1.8	1.4	0.4
MgO	1.2	5.2	6.5	7.7	10.5	13.2	14.3
Na_2O	0.2	0	0.3	0.4	0.4	0.5	0.4
K_2O	0.3	0.3	0.4	1.2	1.1	1.0	0.5
MnO	0.3	0.2	0.3	1.5	1.5	1.4	1.0
SO_3	2.0	2.9	0.7	1.4	1.2	0.4	0.7

2.1 Chemistry of AAS paste in the concrete cover

Thermodynamic modelling simulations conducted in this study for slags activated using various activators including NaOH, Na_2SiO_3, $Na_2O{\cdot}2SiO_2$, Na_2CO_3 and Na_2SO_4 follow very similar procedures to those described by Myers et al. [12–14]. To establish a look-up database for use in further simulations, the masses and volumes of each stable solid phase and the chemical compositions of the aqueous solutions simulated by using the GEMS-Selektor software, were tabulated and stored in MATLAB (hereafter referred to as the 'GEMS calculated database') for a large number of slag compositions. This database is then interrogated directly for calculation of the total chloride binding capacity of the cementitious constituent of each concrete simulated. Additionally, this database included the properties of the modelled C-(N-)A-S-H gel solid solution for each combination of slag and activator, such as composition, density and molar volume. The full database is also presented as Supplementary Information accompanying this paper.

To ensure that the range of chemistries studied here span those that are relevant to AAS, the SiO_2 contents within the simulated slags were fixed at 30 and 40 wt.%, and the effective SO_3 was fixed at 2 wt.% but represented as sulfide; the sulfur was specified as S^{2-} and charge-balanced by H^+. The minor species Na, K and Mn were neglected, and given the passive nature of Fe within slags [15], Fe was excluded from the simulations. The remaining species were specified within the pseudo-ternary system CaO-Al_2O_3-MgO. For fixed quantities of SiO_2 and SO_3, the molar quantities of CaO, Al_2O_3, and MgO were calculated and normalised to constitute the remainder of the slag. Within the pseudo-ternary CaO-Al_2O_3-MgO sub-system, the range $0.5 \leq CaO \leq 1$, $0 \leq Al_2O_3 \leq 0.5$, and $0 \leq MgO \leq 0.5$ (on a molar basis) was covered in the simulation, using a step size of 0.02 in each constituent to span this part of the pseudo-ternary sub-system.

The simulations were carried out at extents of slag reaction from 10 to 60 %, with a step size of 5 %, to ensure coverage of early age and long-term characteristics of AAS. Unreacted slag at each extent of reaction was considered to be inert in the Gibbs energy minimisation protocol. The w/b ratio (water/binder, where the anhydrous activator components are considered part of the binder) was fixed at 0.40 for these simulations. The dosage of the activator was set to 8 g activator/100 g slag for activation by Na_2CO_3 and Na_2SO_4 [12,16], 4.75 g activator/100 g slag for NaOH [17], 10.24 g activator/100 g slag for Na_2SiO_3 (modulus: SiO_2/Na_2O molar ratio = 1.0) [18], and 13.4 g activator/100 g slag for $Na_2O{\cdot}2SiO_2$ (modulus = 2) [17]. The activator doses for NaOH, Na_2SiO_3 and $Na_2O{\cdot}2SiO_2$ activated slags are slightly higher than those reported in the literature. A predominantly $N_{2\,(g)}$ atmosphere was used for the

simulations to provide an oxygen-depleted environment to prevent sulfur oxidation, representing undamaged concrete.

Simulations were carried out using the Gibbs energy minimisation software GEM-Selektor version 3.2 [19,20] (http://gems.web.psi.ch/), with the CEMDATA14 database [21] supplemented by additional phases as described below. Thermodynamic data for solid phases, aqueous species/complexes, and gases considered in this study are listed the Supplementary Information. The aqueous and gas phase models were represented by the Truesdell-Jones version of the extended Debye-Hückel equation (Eq. 1) and the ideal gas equation of state, respectively [12].

$$log_{10}(\gamma_j) = \frac{-A_\gamma z_j^2 \sqrt{I}}{1+\dot{a}B_\gamma\sqrt{I}} + b_\gamma I + log_{10}\frac{x_{jw}}{X_w} \quad \text{(Eq. 1)}$$

where, γ_j and z_j are the activity coefficient and the charge of the j^{th} aqueous species, respectively, I is the ionic strength of the aqueous phase, A_γ ($kg^{0.5}mol^{-0.5}$) and B_γ ($kg^{0.5}mol^{-0.5}cm^{-1}$) are electrostatic parameters that depend on the temperature and pressure, and x_{jw} (mol) and X_w (mol) are the molar quantities of water and total aqueous phase, respectively. The average ionic radius ($\dot{a}$, Å) and the parameter for short-range interactions of charged species (b_γ, kg/mol) were specified according to [22], and set to 3.31 and 0.098 kg/mol respectively, representing NaOH-dominated solutions.

The thermodynamic dataset for solid phases (as indicated in the Supplementary Information) includes the ideal solid solution models CNASH_ss [14] and MA-OH-LDH_ss [13], for the calcium-alkali aluminosilicate hydrate and the hydrotalcite-group layered double hydroxide (LDH) solid solutions, respectively. In addition, zeolites such as natrolite ($Na_{0.4}Al_{0.4}Si_{0.6}O_2{\cdot}0.4H_2O$) and Ca-heulandite ($Ca_{0.111}Al_{0.222}Si_{0.778}O_2{\cdot}0.667H_2O$) have been considered in the thermodynamic simulations and are consistent with experimentally determined phase assemblages in AAS. All other zeolites mentioned in [13] were supressed as they were not observed in initial trial simulations.

As mentioned earlier, thermodynamic simulations were conducted for slags either containing 30 wt. % or 40 wt. % SiO_2. So, the MATLAB input script selects the type of slag to use from the database, initially based on the bulk SiO_2 content and the activator type selected by the user. Therefore, slags with ≥ 35 wt. % SiO_2 were represented by the database entries with 40 wt. % SiO_2, and those with < 35 wt. % SiO_2 were assumed to be similar to those containing 30 wt. % SiO_2. Based on the mole fractions of CaO, MgO and Al_2O_3 present, the SiO_2 content and the activator, the MATLAB script extracts data for the hydrate phase assemblage from the tabulated 'GEMS calculated database' at the selected degree of hydration.

In this study, the sulfur content of the slag, the w/b ratio used to formulate the AAS binder and the paste volume were kept constant, although these parameters do represent scope for future model extension.

2.2 Chloride binding and diffusion

The transport of chloride within concrete under saturated conditions is primarily driven by diffusion, and this is the mechanism described here; other forms of transport such as migration and capillary suction are not considered. Under saturated conditions, the transport of chloride ions can be assumed [23] to occur via the evaporable water in the concrete (w_e – defined in volume fraction terms), which is considered to be the volume of water in the pore solution of the concrete. So, the flux (J_{Cl} , in kg/m^2·s) of chloride ions through the concrete at depth x from the surface can be described by Fick's first law (Eq. 2):

$$J_{Cl} = -D^*_{Cl}\frac{\partial C_f}{\partial x} = -D_{Cl}\cdot w_e \cdot \frac{\partial C_f}{\partial x} \quad \text{(Eq. 2)}$$

where, D_{Cl} (m^2/s) is the effective diffusion coefficient when the chloride concentration is expressed in terms of kg/m^3 of concrete, and D_{Cl}^* (m^2/s) is the effective diffusion coefficient when the chloride concentration is expressed in kg/m^3 of pore solution. The free chloride concentration is represented by C_f (kg/m^3) and the negative sign indicates the difference between the direction of the concentration gradient and the direction of transport. By applying mass conservation in saturated concrete, and substituting Eq. 2 into Eq. 3, the change in the total chloride concentration (C_t , in kg/m^3 of concrete) with respect to time (t) can be expressed as a function of the change in free chloride concentration as a function of the distance within the concrete cover, and is articulated as Fick's second law (Eq. 4) [23,24] when D_{Cl} is assumed to be uniform throughout the cover concrete:

$$\frac{\partial C_t}{\partial t} = -\frac{\partial J_{Cl}}{\partial x} \quad \text{(Eq. 3)}$$

$$\frac{\partial C_t}{\partial t} = \frac{\partial}{\partial x}\left(D_{Cl}\cdot w_e \cdot \frac{\partial C_f}{\partial x}\right) = D_{Cl}\cdot w_e \cdot \frac{\partial^2 C_f}{\partial x^2} \quad \text{(Eq. 4)}$$

The total chloride concentration can be expressed as a function of the free chloride concentration, bound chloride content (C_b), and the total evaporable water as Eq. 5 [25]:

$$C_t = C_b + w_e C_f \quad \text{(Eq. 5)}$$

Substitution of Eq. 5 into Eq. 4 allows consideration of the influence of chloride binding on the diffusion of free chloride ions within the concrete matrix, and the modified equation for Fick's second law can be expressed as Eq. 6:

$$\frac{\partial C_f}{\partial t} = D_{app,Cl} \cdot \frac{\partial^2 C_f}{\partial x^2} \quad \text{(Eq. 6)}$$

and,

$$D_{app,Cl} = \frac{D_{Cl}}{1+\frac{1}{we}\cdot\frac{\partial C_b}{\partial C_f}} \quad \text{(Eq. 7)}$$

where, $D_{app,Cl}$ is the apparent chloride diffusion coefficient (m^2/s) and $\partial C_b/\partial C_f$ is the chloride binding capacity of the concrete cover [23]. As highlighted in Eq. 7, $D_{app,Cl}$ can thus be described (Figure 1) as a function of the chloride binding capacity of the concrete cover. The chloride binding capacity of the cementitious hydrates is dependent on the hydrate phase assemblage, which in turn is a function of the chemistry of the slag and the activating solution, and the degree of hydration. Additionally, as highlighted in Figure 1, $D_{app,Cl}$ can also be influenced by the evolving pore structure of the concrete cover (pore geometry, tortuosity of the bulk paste and the ITZ, connectivity), but these effects fall out of the scope of this study.

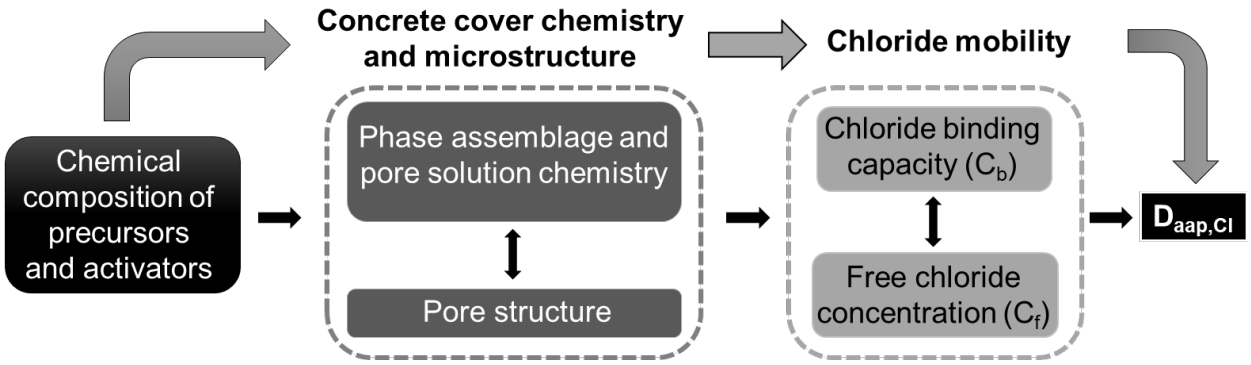

Figure 1: A simple schematic of the factors influencing the effective chloride diffusion coefficient in concrete under saturated conditions.

The extent of chloride binding for a particular phase assemblage can be described as a function of free chloride concentration via chloride binding isotherms (when determined at a given temperature), using functional forms such as the Langmuir [24] and Freundlich isotherms (Eq. 8) [23,26].

$$C_b = \alpha C_f^{\beta} \quad \text{(Eq. 8)}$$

where, α and β are empirical constants and their values depend on the chemistry of the binder. Tang and Nilsson [25] observed that the Langmuir functional form was only valid for

free chloride concentrations less than 0.05 M as it cannot extend beyond the formation of an adsorbed monolayer, but for free chloride concentrations greater than 0.01 M, the use of a Freundlich isotherm was deemed more appropriate [25]. Therefore, the Freundlich adsorption isotherm was used to fit experimental data [7] in this study, and to quantify the binding capacity and apparent chloride diffusion coefficient of AAS; this is revisited later. Eq.8 can be differentiated with respect to C_f to give Eq. 9:

$$\frac{\partial C_b}{\partial C_f} = \alpha\beta C_f^{\beta-1} \quad \text{(Eq. 9)}$$

Substituting Eq. 9 into Eq. 7, Eq.10 is obtained:

$$D_{app,Cl} = \frac{D_{Cl}}{1+\frac{1}{w_e}\cdot\alpha\beta C_f^{\beta-1}} \quad \text{(Eq. 10)}$$

Both long- and short-term tests have been used to quantify chloride ingress within concrete structures; however, one of the most accepted methods is the rapid chloride migration (RCM) test, NT Build 492 [27], developed by Tang [28]. The RCM test is a short-term test and gives the value of non-steady state migration coefficient (D_{nssm} or D_{RCM}) and details of the test can be found in [27,28]. The DuraCrete guidelines [29,30] use $D_{RCM}\ (t)$ as an input parameter to define the service life of concrete structures, implying that this should be equivalent to $D_{app,Cl}$ values obtained using bulk diffusion tests. However, in the case of PC-based concretes, several authors [28,31–33] have found the value of D_{RCM} to be slightly higher than $D_{app,Cl}$, and it is possible that the short-term RCM test underestimates the extent of chloride binding in cement matrices. This has been found to be true in the case of AAS mortars as well [6], where the ratio of the non-steady state migration and apparent diffusion coefficients ($D_{RCM}/D_{app,Cl}$) was found to be approximately 100. Therefore, the value of D_{Cl} in Eq. 10 in this study was assumed to be the mean D_{nssm} (0.5×10^{-12} m^2/s) obtained using the NT Build 492 test on Na_2SiO_3-activated M6 mortars cured for 28 days, reported in [7] and [6], implying that D_{nssm} obtained using NT Build 492 does not take into account the influence of chloride binding. The value of D_{Cl} was assumed to be the same for all AAS considered in this study. The experimentally observed D_{nssm} values for AAS mortars [7] were considered to be true for AAS concretes as well, on the assumption that the aggregate volume fraction (or the interfacial transition zone (ITZ)) has negligible influence on $D_{app,Cl}$ [34]. Future evolution of the model is envisaged to include a more sophisticated treatment of aggregate volume and ITZ effects, but that is beyond the scope of the current work.

AAS binders are characterised by the formation of C-(N-)A-S-H gel as the major reaction product, and secondary reaction products including hydrotalcite-like Mg-Al-OH-LDH phases and AFm-group phases. As an initial assumption, the total binding capacity of AAS can be

approximated by the sum of the individual binding capacities of its constituent hydrate phases (Eq. 11).

$$\left(\frac{\partial C_b}{\partial C_f}\right)_{\substack{total\\binder}} = \left[\left(\frac{\partial C_b}{\partial C_f}\right)_{C\text{-}(N\text{-})A\text{-}S\text{-}H} + \left(\frac{\partial C_b}{\partial C_f}\right)_{Mg\text{-}Al\text{-}OH\text{-}LDH} + \left(\frac{\partial C_b}{\partial C_f}\right)_{strätlingite} + \ldots\right] \quad \text{(Eq. 11)}$$

According to Eq. 11, if the amounts and the individual chloride binding capacity of each of the reaction products are known, a theoretical value for the total chloride binding capacity of AAS could be calculated. Ke [7] calculated the individual chloride binding capacities of the C-(N-)A-S-H gel, hydrotalcite-like Mg-Al-OH-LDH phase and strätlingite, under pH conditions relevant to the pore solution chemistry of AAS. Substituting Eq. 11 into Eq. 7, $D_{app,\,Cl}$ can be represented by Eq. 12:

$$D_{app,Cl} = \frac{D_{Cl}}{1+\frac{1}{w_e}\cdot\left[\left(\frac{\partial C_b}{\partial C_f}\right)_{C\text{-}(N\text{-})A\text{-}S\text{-}H} + \left(\frac{\partial C_b}{\partial C_f}\right)_{Mg\text{-}Al\text{-}OH\text{-}LDH} + \left(\frac{\partial C_b}{\partial C_f}\right)_{strätlingite} + \ldots\right]} \quad \text{(Eq. 12)}$$

Based on the individual binding isotherms obtained by Ke [7] (reproduced in Figure 2), the total chloride binding capacity of each AAS composition in this study was considered to be the sum of the individual binding capacities of the C-(N-)A-S-H gel, hydrotalcite-like Mg-Al-OH-LDH phase, and the AFm phase strätlingite. The latter phase is predicted extensively in thermodynamic simulations of AAS, although less often observable as a crystalline phase by X-ray diffractometry [35,36]. Additional phases formed in smaller quantities in AAS, such as monocarbonate-AFm, monosulfate-AFm, ettringite, Ca-heulandite, natrolite, katoite and brucite, were not included in the calculations of chloride binding. Various authors have determined chloride binding isotherms for synthetic AFm phases [37–39], however, they are not considered in this study primarily because the experimental setup used to calculate the binding isotherms could neither represent the alkalinity nor the ionic strength of the pore solutions of AAS.

Figure 2: Chloride binding isotherms for synthetic phases formed in AAS, C-(N-)A-S-H gel, hydrotalcite-like Mg-Al-OH-LDH phase and strätlingite; data from Ke [7]. The experimental methods used to determine bound and free chloride are detailed in [7,8]. It must be noted that chloride binding in AAS could occur via the physical adsorption of chloride on the surface of the different reaction products and ionic exchange with the interlayer anionic species present in some reaction products [7,8].

Ke [7] reported the experimental chloride binding capacity of Na_2SiO_3- and Na_2CO_3-activated slag (composition M6, Table 1). In the current study, the experimentally determined binding isotherm for Na_2SiO_3-activated M6 from that work [7] is also assumed to be valid for slag M6 activated using the other activators discussed (NaOH, $Na_2O{\cdot}2SiO_2$, Na_2CO_3, and Na_2SO_4), due to the lack of experimental binding isotherms in the literature for various AAS. In addition, Ke [7] compared the theoretical (Eq. 11) and experimental chloride binding isotherms, and observed the theoretical values to be 3 to 6 times higher than experimental observation. This overestimation was attributed to the higher crystallinity of the synthetic phases used for measuring the individual chloride binding isotherms [7]. It is also possible that

surface blocking by neighbouring hydrate phases influences these results, when comparing finely-dispersed synthetic powders to hydrated pastes. Based on the quantities of C-(N-)A-S-H gel, hydrotalcite-like Mg-Al-OH-LDH phase and strätlingite predicted by the thermodynamic simulations as described in Section 2.1, the total chloride binding isotherm for each AAS considered in this study was calculated as the sum of the individual chloride binding capacities of each of these phases (as shown in Figure 3A) in proportions corresponding to a slag reaction extent of 60 %. This methodology was followed in scaling down the theoretical binding isotherms of activated M6 binders to match the experimentally determined values. In the absence of any experimental information to indicate otherwise, the theoretical binding isotherms for all other activated slags (M1, M5, M8, M11, M13 and M14) and for all activators were also scaled down by the same factor (as shown in Figure 3B). In reality it is likely that the scaling factors between synthetic phases and real pastes will depend on the slag and activator chemistry, but given that no data currently exist to describe this dependence, it is neglected in the current work.

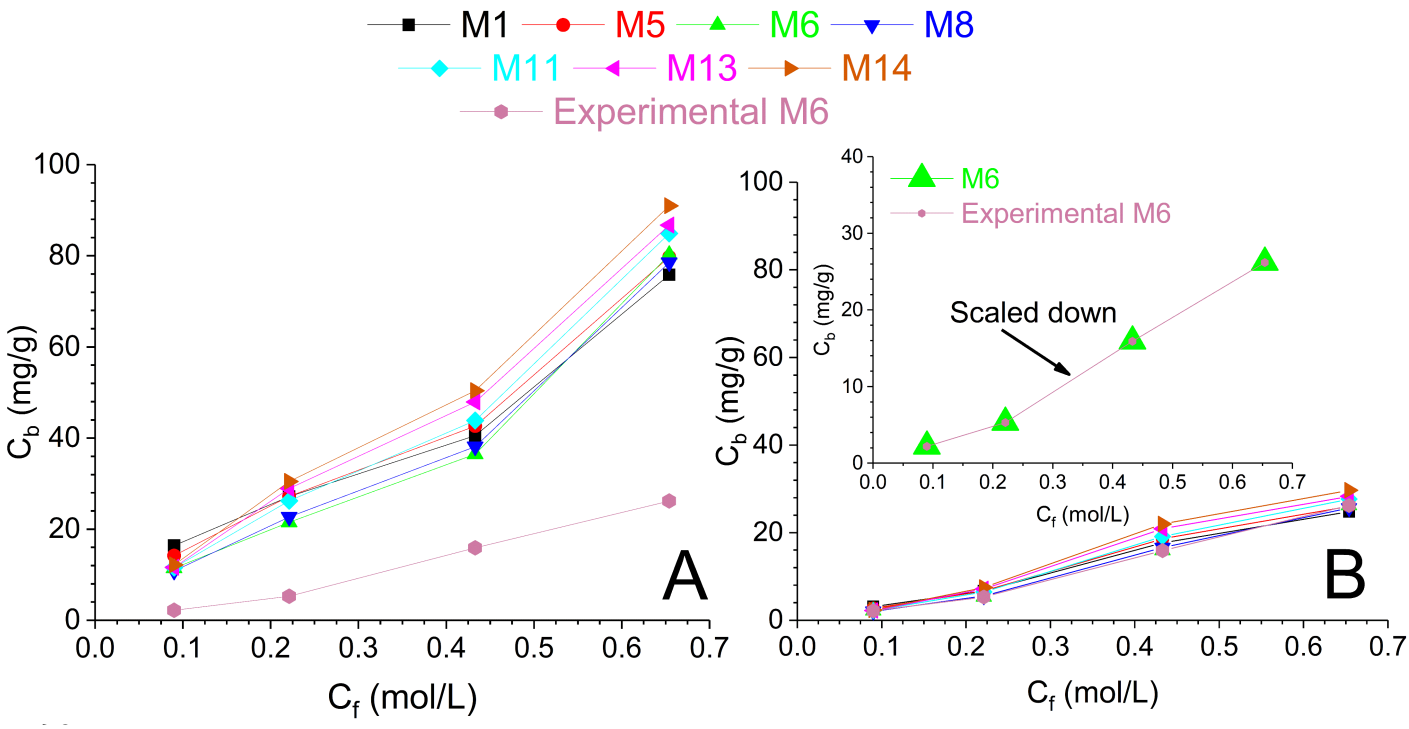

Figure 3: (A) Chloride binding isotherms calculated through the use of simulated solid phase assemblages for Na_2SiO_3-activation of all slags considered in this study at 60% reaction extent, and the individual binding capacity of each of the reaction products, compared with the experimental data from [7]. (B) Scaling down of the theoretical chloride binding isotherms to match experimental data, defining the apparent diffusion coefficients as a function of the free chloride concentration.

303

304 To model the diffusion of chloride in saturated concretes, considering $D_{app,Cl}$ as a function
305 of C_f, Eq. 7 was solved numerically as a space-time problem using the explicit finite difference
306 method [40], in one spatial dimension with time and space steps set to approximately 1 day and
307 1 mm, respectively. To take into account the non-linear nature of $D_{app,Cl}$ (C_f), the value of $D_{app,Cl}$
308 was set to depend on the free chloride concentration at the previous spatial step for any given
309 time step, and was calculated individually at each space-time step using the calculated binding
310 parameters of the Freundlich isotherm. It is assumed that the timescales of the chloride binding
311 and chloride diffusion processes can be fully decoupled from each other, as the kinetics of
312 chloride binding are rapid compared to the kinetics of diffusion - i.e., the adjustment of the
313 bound/free chloride ratio to small changes in chloride concentration per timestep is assumed to
314 be essentially instantaneous [41].

315 Figure 4 shows the finite difference propagation model used. It is important to note that the
316 calculated Freundlich adsorption isotherm is only validated for free chloride concentrations
317 lower than 0.654 M, as binding isotherms for higher free chloride concentrations do not exist
318 in the literature. For a concrete with thickness L, the initial and boundary conditions used to
319 solve Eq. 7 numerically are described by Eq. 13:

320 For $t \geq 0$, $C_f = C_o$ at $x = L$

321 $C_f = C_s$ at $x = 0$ (Eq. 13)

322 For $t = 0$, $C_f = C_o$ at $x > 0$

323 where, C_o is the chloride concentration present in the concrete prior to exposure to a salt
324 solution (defined in wt.% of the binder; set to zero for the simulations presented here), and C_s
325 is the concentration of chloride in the exposure salt solution (0.60 M Cl^-). The maximum
326 thickness (L) of the concrete was set to be 70 mm. It must be noted that the surface chloride
327 concentration for each AAS was assumed to be constant, and the influence of leaching [30] (or
328 any other factors that could potentially lead to a reduction in the near-surface alkalinity) on the
329 chloride binding capacity of the hydrate phases was not considered in this study. Based on the
330 total amount of evaporable water content in each of the AAS phase assemblages, the surface
331 chloride concentration was calculated in terms of wt.% of binder.

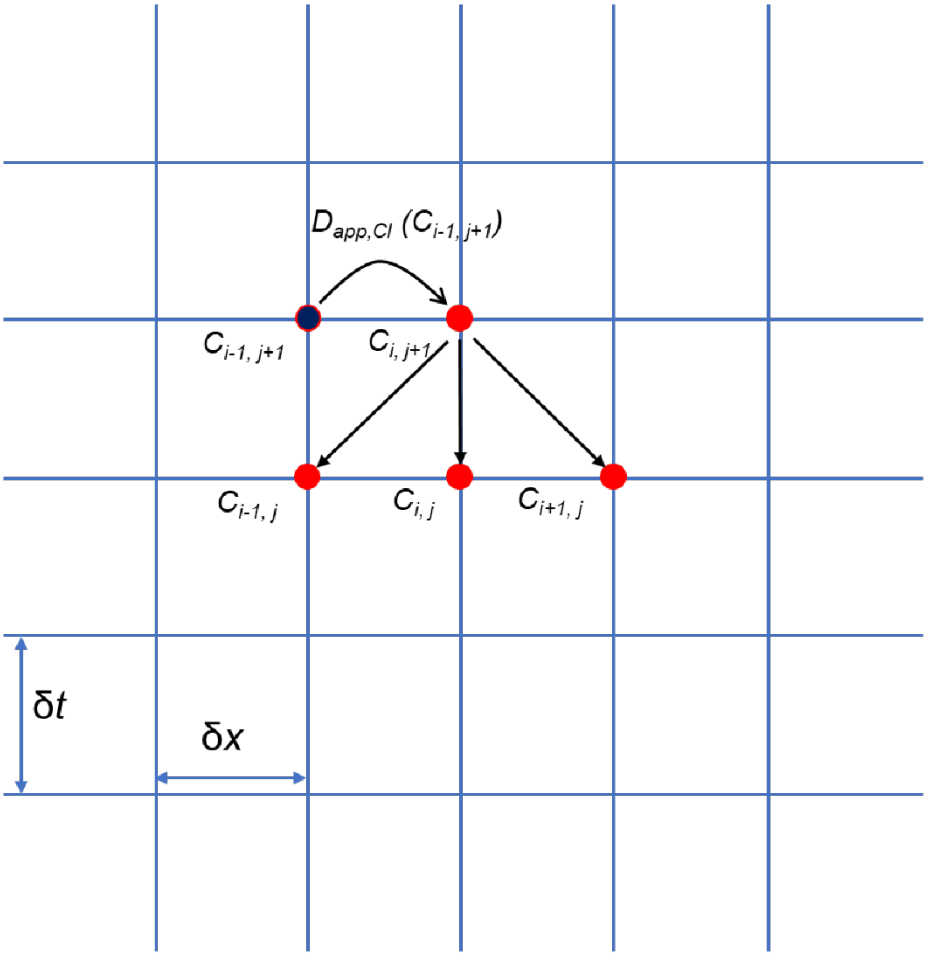

Figure 4: Schematic diagram of the explicit fine difference method employed in this study to describe the ingress of chloride as a space-time problem. The values of δx and δt were set to 1 mm and 0.9125 days, respectively, making the grid (x vs. t) size 70 × 28,000, representing a cover depth of 70 mm and 70 years of service-life. The explicit fine difference method was solved using a loop function over space and time, with the boundary conditions described in Eq. 13. $D_{app,Cl}$ was calculated based on the Freundlich isotherm, binder chemistry, and free water content, and expressed as a function of the free chloride concentration ($\boldsymbol{c}_{i-1,j+1}$) of the previous space step $i - 1$. The free chloride concentration ($\boldsymbol{c}_{i,j+1}$) at time step ($j + 1$) was thus calculated on the basis of free chloride concentrations ($\boldsymbol{c}_{i,j}$, $\boldsymbol{c}_{i-1,j}$, and $\boldsymbol{c}_{i+1,j}$,) at the previous time step j at locations i, $i - 1$ and $i + 1$, using the assumption of separation of time-scales between the binding (fast) and diffusion (slow) processes.

3 Results and Discussion

3.1 Chemistry of the concrete cover

Figure 5 shows the influence of MgO content in the slag and the type of activator on the simulated solid phase assemblages of AAS at 60 % extent of slag reaction. Irrespective of the nature of the activator and of the MgO content in the slag, the hydration products of AAS are dominated by a C-(N-)A-S-H gel (Figure 5), however, the bulk MgO content in the slag significantly influences the chemistry of the C-(N-)A-S-H gel. The Ca/Si ratio in the C-(N-)A-S-H gel for all AAS systems studied, at 60 % extent of slag reaction, was calculated to be between 0.80 and 1.07. Lower MgO content in the slag leads to a higher Al content in the C-(N-)A-S-H gel; during the reaction of MgO-rich slags, much of the Al is consumed in the formation of secondary hydration products such as hydrotalcite-like phases [18], resulting in low Al/Si ratios in the C-(N-)A-S-H gel, Figure 5.

In NaOH-activated slags, the secondary reaction products were Mg-Al-OH-LDH, katoite (C_3AH_6) and strätlingite (C_2ASH_8). At low MgO contents, for example in slags M1 and M5, the secondary hydration products are dominated by the formation of katoite and strätlingite. However, at higher slag MgO content, hydrotalcite-like Mg-Al-OH-LDH phase dominates the secondary hydration products, with trace katoite and strätlingite. The presence of katoite in this study was only observed for Ca-rich slags with Ca/Si $\geq$ 1.14 (M1, M5 and M6) and this observation aligns well with the literature [12,42,43]. Strätlingite is also a minor constituent observed in NaOH-activated slags with low MgO contents [44], and its stability in C-(A-)S-H systems at low temperatures (around 20 °C) was confirmed by Okoronkwo and Glasser [45]. Trace quantities of natrolite ($Na_{0.4}Al_{0.4}Si_{0.6}O_2{\cdot}0.4H_2O$) and brucite ($Mg(OH)_2$) were predicted to form in slags containing high amounts of MgO; M13 and M14, respectively. The prediction of brucite in the solid phase assemblages of slags activated using NaOH, and also Na_2SiO_3 and $Na_2O{\cdot}2SiO_2$ in this study (see below), is in contradiction with experimental observations for AAS [11,17,43,46–49]. This could possibly be explained by the lack of thermodynamic data for MgO-SiO_2-H_2O (magnesium silicate hydrate or M-S-H) phases in the CEMDATA14 database used in this study, as there is not another stable Mg-containing phase available to take up this element once the capacity to form Mg-Al-OH-LDH has been exhausted by consumption of all available Al.

In Na_2SiO_3-activated and $Na_2O{\cdot}2SiO_2$-activated slags (Figure 5B and Figure 5C, respectively), the secondary hydration products are the hydrotalcite-like Mg-Al-OH-LDH phase, natrolite, strätlingite, Ca-heulandite, katoite and brucite. Similar to the observations made for NaOH-activated slags, the quantity of Mg-Al-OH-LDH formed was strongly dependent on the slag MgO content (Figure 5B, C). In slags containing 30 wt. % SiO_2 and low

bulk MgO contents (M1 and M5) activated using Na_2SiO_3 and $Na_2O{\cdot}2SiO_2$, strätlingite was the major secondary reaction product, with minor and trace quantities of katoite, respectively, also being present. Ca-heulandite was only predicted to form in slags containing 40 wt. % SiO_2 and high MgO contents (M6 to M14), and was more pronounced in $Na_2O{\cdot}2SiO_2$-activated slags (Figure 5B and Figure 5C), due to the higher Si content provided by this activator. Similarly, natrolite was also predicted to form for slags containing 40 wt. % SiO_2 and high MgO contents (M6 to M13). As mentioned above, brucite is also predicted to form in trace quantities in Na_2SiO_3- and $Na_2O{\cdot}2SiO_2$-activation of slags containing a high level of MgO (M14).

Figure 5: Influence of bulk MgO content in slags, and the type of activator in the simulated solid phases when the extent of slag reacted is 60 %. The values in square [ ] and curly brackets { } within the navy-blue background indicate the calculated Ca/Si and Al/Si ratios in the C-(N-)A-S-H gel, respectively. $C_4A\underline{c}H_{11}$ = monocarbonate-AFm, $C_4A\underline{s}H_{12}$ = monosulfate-AFm, Mg-Al-OH-LDH = hydrotalcite-like phase, C-(N-)A-S-H gel = calcium (alkali) aluminosilicate hydrate gel.

In Na_2CO_3-activated slags (as shown in Figure 5D), the hydrotalcite-like phase (Mg-Al-OH-LDH), natrolite, monocarbonate-AFm ($C_4A\underline{c}H_{11}$) and calcite ($CaCO_3$) were predicted to form. Additionally, in slags with 40 wt. % SiO_2 and extremely high bulk MgO content (M13 and M14), brucite and Ca-heulandite were observed to form. Similar to NaOH, Na_2SiO_3, and $Na_2O{\cdot}2SiO_2$-activated slags, the formation of hydrotalcite-like phase was dependent on the extent of slag reaction and the bulk MgO content of the slag. The formation of natrolite was predicted for all slags considered in this study, and it indicates the coexistence of C-(N-)A-S-H and N-A-S-H type gels [46]. Monocarbonate-AFm is predicted to form in Na_2CO_3-activated slags, as observed experimentally [16], and its formation was closely associated with the bulk MgO and SiO_2 content in the slag (Figure 5D), being preferred in slags with lower MgO and/or lower SiO_2 contents. Additionally (as seen in Figure 5D), in slags with high bulk MgO content and ~40 wt. % SiO_2 (M13 and M14), Ca-heulandite and brucite were predicted to form in trace quantities. Unlike NaOH, Na_2SiO_3 and $Na_2O{\cdot}2SiO_2$-activated slags, katoite and strätlingite were not predicted to form in Na_2CO_3 activation.

In Na_2SO_4-activated slags (Figure 5E), the secondary reaction products were ettringite ($C_6A\underline{s}_3H_{32}$), monosulfate-AFm ($C_4A\underline{s}H_{12}$), hydrotalcite-like Mg-Al-OH-LDH, strätlingite, natrolite, brucite and Ca-heulandite. Ettringite has been observed experimentally to be the major secondary reaction product in Na_2SO_4-activated slags [50–53], and is primarily responsible for the higher solids volume of these binders than other activated slags. Ettringite was stable for the entire range of slags (M1 to M14) studied here (Figure 5E), but more prevalent for slags with higher bulk SiO_2 content. In contrast, for lower-SiO_2 slags, monosulfate-AFm and strätlingite were observed to be the most stable secondary reaction products. The hydrotalcite-like phase was much less prevalent for slags with low MgO contents and with 30 wt. % SiO_2 (M1 and M5) when compared to their higher SiO_2 and higher MgO counterparts (M6 to M14). Natrolite and Ca-heulandite were predicted to be minor products, and small amounts of brucite were again predicted to form in slags with very high bulk MgO contents (M13 and M14).

3.2 Chloride diffusion

Based on the simulated solid and aqueous phase assemblages at 60 % extent of slag reaction from Section 3.1, chloride binding isotherms for each AAS were calculated, so they could be utilised to calculate the apparent chloride diffusion coefficient as a function of the free chloride concentration, and to estimate the ingress of chloride in each of these binders.

3.2.1 Influence of chloride binding

Figure 6 shows a representative example depicting the influence of chloride binding on the calculated chloride ingress profiles; in this instance, for concretes made from Na_2SiO_3-activated M6 at various ages of exposure. As mentioned in Section 2.2, it must also be noted that the migration coefficient (D_{nnsm}) obtained in [7] was assumed to underestimate chloride binding occurring within AAS, and therefore has been considered to be the value to be used when there is no chloride binding. Chloride binding significantly retards the transport of chloride towards the steel-concrete interface, and its importance can be clearly seen in chloride profiles modelled at later ages (Figure 6D). Chloride binding decreases the concentration of free chloride ions in the pore solution that are available to diffuse through the material [28,54,55]. Therefore, the use of D_{nssm} as a parameter to characterise the ingress of chloride may lead to underestimation of the service life of concrete structures based on AAS.

One of the major advantages of relating the $D_{app,Cl}$ to the binding capacity of each of the reaction products present in a concrete structure, is the avoidance of the mathematically problematic usage of an empirically derived time-dependent diffusion coefficient together with Fick's equations, as is used by many service-life guidelines [29,30]. Table 2 shows the calculated binding constants of the Freundlich adsorption isotherm, and the thermodynamically estimated evaporable water content expressed as volume % of the total binder (i.e., the volume % of the binder that is H_2O in the pore solution, from the thermodynamic simulations presented as Supplementary Information, assuming negligible difference in the effective volume of pore solution in the binder between pastes and concretes), which are used to derive a relationship between $D_{app,Cl}$ and the free chloride concentration for various AAS compositions when the extent of slag reaction is 60 %. The values of α and β Freundlich adsorption isotherm parameters obtained by fitting the chloride binding isotherms are only validated for free chloride concentrations up to 0.654 M, which is the limit of the experimental data set used [7]. The binding parameter β calculated for all activated slags was greater than 1, which suggests that much of the chloride binding in AAS occurs via chemisorption rather than physical adsorption in the concentration range for which data are available [56,57].

Table 2: Fitted chloride binding constants (Freundlich isotherm parameters) and the evaporable water contents (un-bound H_2O) that were used to determine $D_{app,Cl}$ for each space and time step, for each slag and activators assessed at 60 % extent of slag reaction.

	NaOH			**Na_2SiO_3**			**$Na_2O{\cdot}2SiO_2$**		
	A	***β***	**Evaporable water (vol.%)**	***α***	***β***	**Evaporable water (vol.%)**	***α***	***β***	**Evaporable water (vol.%)**
M1	0.29	1.22	36.6	0.85	1.08	32.5	1.32	1.03	30.8
M5	0.27	1.33	35.5	0.67	1.17	32.6	1.05	1.11	31.3
M6	0.46	1.28	36.8	0.46	1.28	36.7	0.46	1.28	36.7
M8	0.56	1.26	35.7	0.44	1.29	36.0	0.45	1.29	35.9
M11	0.40	1.36	36.5	0.48	1.31	35.0	0.48	1.30	35.0
M13	0.42	1.37	35.5	0.49	1.32	34.0	0.49	1.32	34.2
M14	0.41	1.37	35.2	0.51	1.32	33.9	0.47	1.31	34.8

	Na_2CO_3			**Na_2SO_4**		
	α	***β***	**Evaporable water (vol.%)**	***α***	***β***	**Evaporable water (vol.%)**
M1	0.25	1.22	29.8	0.85	1.06	26.4
M5	0.36	1.28	30.3	0.61	1.20	26.1
M6	0.46	1.28	38.1	0.46	1.28	26.9
M8	0.46	1.29	37.8	0.45	1.29	26.1
M11	0.51	1.31	37.3	0.51	1.30	26.0
M13	0.52	1.32	36.3	0.43	1.31	26.3
M14	0.53	1.32	36.4	0.36	1.27	27.3

Figure 6 also compares the influence of using a constant value of $D_{app,Cl}$, calculated based on the maximum chloride binding capacity of a binder (blue dotted line), and the $D_{app,Cl}$ dependent on the free chloride concentration, calculated based on the Freundlich adsorption isotherm (red dashed line). As seen in Figure 6, using a fixed diffusion coefficient and assuming the highest chloride binding capacity (calculated using the Freundlich adsorption isotherm) to be true for all concentrations of free chloride and through the entire depth of the concrete cover overestimates the extent of chloride binding when the free chloride concentration is low, and also overestimates the time taken for chloride to reach a potentially damaging concentration at the depth of the first steel reinforcing element.

For example, for a cover depth of 20 mm and the chloride 'threshold' value of 0.2 wt. % of binder, the influence of chloride binding on the predicted initiation time for a steel-reinforced concrete structure based on Na_2SiO_3-activated M6 can be determined using the model presented here. A previous publication [9] by some of the authors of this study shows that the chloride 'threshold' value for steel immersed in simulated pore solutions of AAS is highly dependent on the concentration of sulfide, and additionally, chloride 'threshold' values for steel embedded in AAS mortars/concretes are not available in the literature. Therefore, the chloride 'threshold' value of 0.2 wt. % of binder assumed in this section is only for demonstrative purposes and does not in any way suggest that the chloride threshold value for AAS concretes is the abovementioned value. This is quite a low value to assume for a chloride threshold in reinforced concrete, which is done solely for purposes of conservatism.

In the case of no chloride binding and $D_{app,Cl}$ being set equal to D_{nnsm}, the initiation time (defined as the time to reach 0.2 wt. % Cl^- at a depth of 20 mm) was found to be ~15 years, compared to ~70 years when assuming the maximum binding capacity to hold for the entire depth of the concrete cover and using a fixed diffusion coefficient. However, when $D_{app,Cl}$ was related to the free chloride concentration (according to calculated binding isotherms), the initiation time was ~50 years. Logically, the most appropriate way of determining the ingress of chloride would be to relate the $D_{app,Cl}$ to the free chloride concentration by the use of experimentally observed chloride binding isotherms. Unfortunately, experimental chloride profiles for multi-year exposure of reinforced AAS to chloride under saturated conditions (as required for pure diffusional mass transport) are not available in the open literature, and therefore, the direct validation of the modelling results with experimental data was not possible.

Figure 6: Influence of chloride binding on the chloride ingress profiles calculated for Na_2SiO_3-activated M6 at (A) 1 year, (B) 5 years, (C) 10 years and (D) 50 years. The solid lines represent the case of no binding, with the apparent diffusion coefficient assumed to be the migration coefficient obtained from NT Build 492 [7]. The red dashed lines represent the case when the apparent diffusion coefficient was calculated using the free chloride concentration (based on the Freundlich adsorption isotherm) at the preceding space step for any given time step. The dotted blue lines represent the scenario when the apparent diffusion coefficient was kept constant and calculated using only the maximum chloride binding capacity of the AAS paste.

3.2.2 *Influence of slag composition*

Figure 7 shows the influence of the slag composition on chloride ingress after 25 years of exposure to 3.5 wt.% (0.6 M) NaCl solution, calculated for activation of four selected slags by NaOH (Figure 7A), Na_2SiO_3 (Figure 7B), $Na_2O{\cdot}2SiO_2$ (Figure 7C), Na_2CO_3 (Figure 7D) and Na_2SO_4 (Figure 7E).

In the case of NaOH-activated slags (Figure 7A), an increase in the bulk MgO content of the slag leads to retardation in the chloride ingress, indicating a higher chloride binding capacity for NaOH-activated slags with higher MgO content. In slags with lower MgO content and higher CaO content, as in the case of NaOH-activated M1, the chloride binding capacity of the binder is primarily governed by the amounts of strätlingite and C-(N-)A-S-H gel formed. However, in the case of intermediate and high MgO slags, as in NaOH-activated M6, M11 and M14, the precipitation of greater amounts of hydrotalcite-like Mg-Al-OH LDH (Figure 7A) increases the total chloride binding capacity, thereby retarding the ingress of chloride.

According to the quantities of each reaction product (Figure 5A) and the individual binding isotherms of C-(N-)A-S-H gel, hydrotalcite-like Mg-Al-OH LDH phase and strätlingite obtained experimentally by Ke [7], as shown in Figure 2, at relatively high or low concentrations of free chloride, the total binding capacity of the binder would be primarily dominated by the C-(N-)A-S-H gel. However, at intermediate concentrations of free chloride, much of the chloride binding is due to ion-exchange and physical adsorption to Mg-Al-OH LDH and strätlingite (Figure 2). This is true for all of the NaOH-activated slags. For constant exposure to 3.5 wt. % NaCl solution, the calculated near-surface chloride content was found to only marginally change for all NaOH-activated slags shown in Figure 7A. This is primarily due to the similar amounts of evaporable water calculated (as observed in Figure 7A) for each of the binders at 60 % extent of slag reaction.

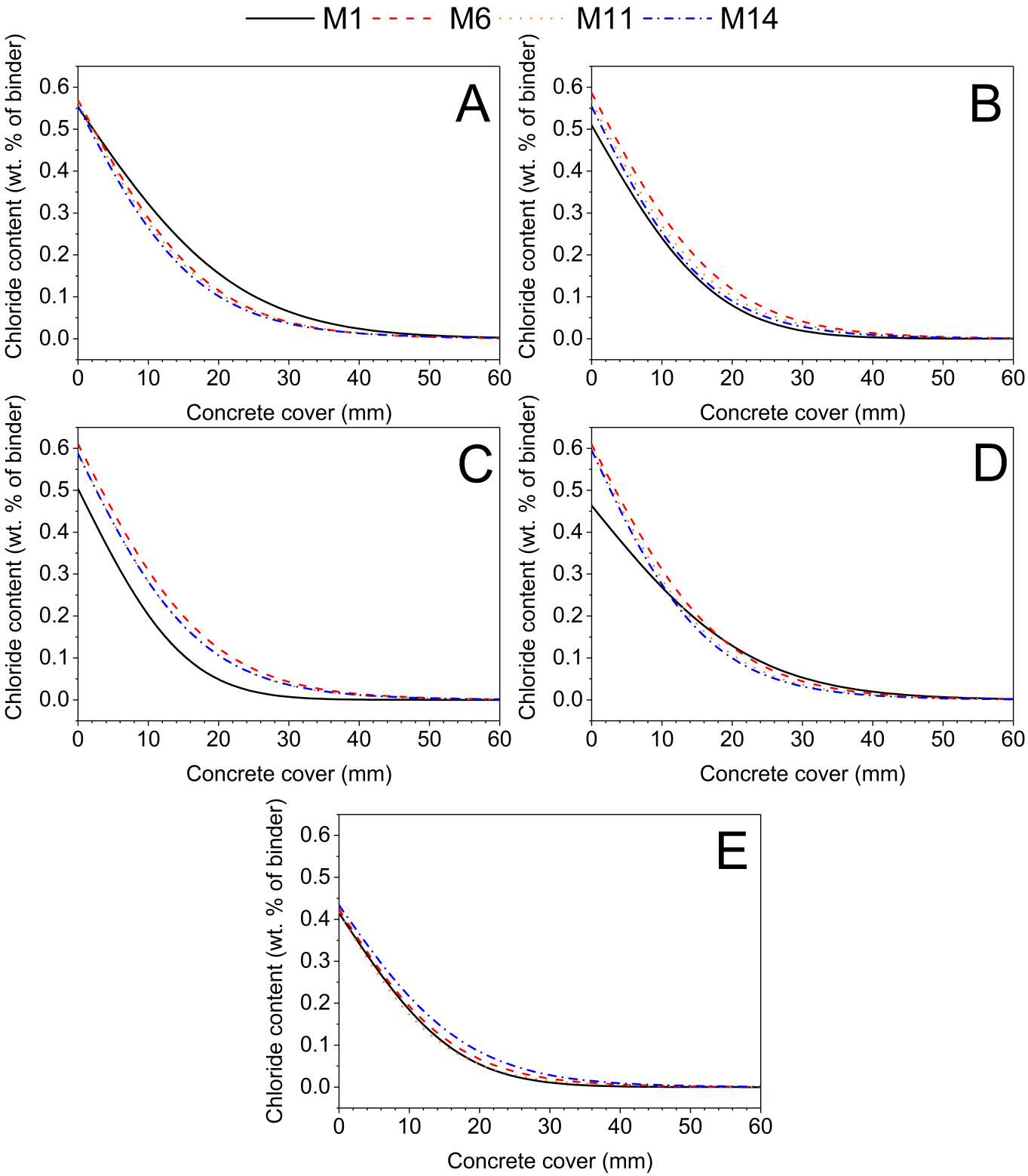

533 Figure 7: Influence of the slag composition on chloride ingress profiles calculated for (A)
534 NaOH, (B) Na_2SiO_3, (C) $Na_2O{\cdot}2SiO_2$, (D) Na_2CO_3 and (E) Na_2SO_4 activated M1, M6, M11
535 and M14 at 25 years of exposure to 0.6 M NaCl solution.

Unlike NaOH-activated slags, in the case of Na_2SiO_3- and $Na_2O{\cdot}2SiO_2$-activated slags (Figure 7B and Figure 7C, respectively) chloride ingress was found to be the slowest in the case of slag M1, when compared to M6, M11 and M14. Figure 7B reveals that at high concentrations of free chloride the extent of chloride binding (depending on the slope, $\Delta c/\Delta x$, of the chloride ingress profiles) is slightly higher in the case of Na_2SiO_3-activated M1 when compared to Na_2SiO_3-activated M6, M11 and M14, with the inverse being true at intermediate and low concentrations of free chloride. However, the binding capacity was found to be much higher at all concentrations of free chloride in the case of $Na_2O{\cdot}2SiO_2$-activated M1 (Figure 7C), when compared to $Na_2O{\cdot}2SiO_2$-activated M6, M11 and M14. In both Na_2SiO_3- and $Na_2O{\cdot}2SiO_2$-activated M1, the lower rates of chloride ingress could be attributed to the higher amounts of strätlingite predicted to form (Figure 5B and Figure 5C). Therefore, in slags with low MgO and high Al_2O_3 contents (e.g. slag M1) activated using Na_2SiO_3 and $Na_2O{\cdot}2SiO_2$, the extent of chloride binding is strongly influenced by the chloride ion-exchange and chloride adsorption capabilities of the AFm-type phases present. Much of the chloride binding in Na_2SiO_3 and $Na_2O{\cdot}2SiO_2$-activated M1 was due to the C-(N-)A-S-H gel and strätlingite, and only a small percentage of the total bound chloride was due to the hydrotalcite-like Mg-Al-OH LDH phase as this was present in only very low quantities in this particular AAS.

In the cases of Na_2SiO_3- and $Na_2O{\cdot}2SiO_2$-activated M6, M11 and M14, chloride binding only took place in the C-(N-)A-S-H gel and hydrotalcite-like Mg-Al-OH LDH phase, as strätlingite is not predicted to form. Similar to the observations in Figure 7A, chloride binding was found to be the highest for slags (among M6, M11 and M14) containing higher bulk MgO contents, and consequently these show slower chloride ingress. The surface chloride concentration was found to be much lower for Na_2SiO_3- and $Na_2O{\cdot}2SiO_2$-activated M1, when compared to the Na_2SiO_3 and $Na_2O{\cdot}2SiO_2$-activated M6, M11 and M14, primarily due to the lower volume of evaporable water (Figure 5B,C).

In the case of Na_2CO_3-activated slags (Figure 7D), the extent of chloride binding was proportional to the bulk MgO content in the slag and thus the amount of hydrotalcite-like Mg-Al-OH-LDH phases. Na_2CO_3-activated M14 exhibited the slowest chloride ingress, followed by Na_2CO_3-activated M11, Na_2CO_3-activated M6 and Na_2CO_3-activated M1. In Na_2CO_3-activated slags, chloride binding occurs only due to the presence of the C-(N-)A-S-H gel and the hydrotalcite-like Mg-Al-OH LDH phase, as no strätlingite was predicted to be formed (Figure 5D). However, in the cases of Na_2CO_3-activated M1 and M6, where monocarbonate-AFm forms as a major and minor reaction product (Figure 5D) respectively, the total chloride binding capacity could be underestimated in these calculations because chloride binding by

monocarbonate was not considered in the absence of binding isotherm data for the relevant pH range. Ke et al. [58] investigated the chloride binding capacity of Na_2CO_3-activated slags, and observed the transformation of monocarbonate to two polymorphs of Friedel's salt via the partial exchange of interlayer CO_3^{2-} by Cl^- in the AFm structure [58–60]. Therefore, chloride binding isotherms for monocarbonate and full characterisation of these anion exchange equilibria (which will also involve competition from hydroxide ions and from various sulfur-containing anions) in simulated pore solutions representative of AAS are required to accurately predict the chloride ingress in these binders. Additionally, in carbonate-bearing pore solutions, the binding capacity of the hydrotalcite-like phase Mg-Al-OH-LDH phase has been observed to be reduced due to the higher affinity of the hydrotalcite-like phase to incorporate divalent ions (CO_3^{2-}) instead of monovalent ions [8,61]. Therefore, in Na_2CO_3-activated slags where the pore solution contains CO_3^{2-}, the extent of chloride binding due to hydrotalcite-like Mg-Al-OH LDH phase is possibly overestimated in these calculations.

For Na_2SO_4-activated slags (Figure 7E), the amount of chloride binding decreases with an increase in bulk MgO content in slag (except for Na_2SO_4-activated M11). Significant amounts of strätlingite are predicted to form in Na_2SO_4-activated M1 (Figure 5E), which might contribute to its higher chloride binding capacity when compared to Na_2SO_4-activated M6 and M14. As mentioned earlier for the case of monocarbonate, the chloride binding capacities of additional phases formed during Na_2SO_4 activation of slags, such as monosulfate and ettringite, have not been considered. The transformation of monosulfate to Friedel's salt in PC based binders is well known [38,39], but chloride binding isotherms in simulated pore solution compositions representative of AAS do not exist in the literature. The ability of ettringite to bind chloride ions has also been debated in the literature [37,39,62]. Therefore, the calculations of the total chloride binding capacity of Na_2SO_4-activated M1 conducted in this study can plausibly be assumed to be underestimated, which means that predictions of the time at which the chloride threshold will be exceeded would be conservative. Na_2SO_4-activated slag M11 exhibited the slowest chloride ingress among all the Na_2SO_4-activated slags due to the higher amounts of C-(N-)A-S-H gel and hydrotalcite like Mg-Al-OH-LDH phases formed in these binders in comparison to Na_2SO_4-activated slags M1, M6, and M14, and consequentially leading to a higher chloride binding capacity. Additionally, the lower chloride binding capacity of Na_2SO_4-activated slag M14 is due to the precipitation of brucite, which was not considered to contribute towards chloride binding. The near-surface chloride concentration in the case of Na_2SO_4-activated slags in Figure 7E is much lower than those observed for other activators in Figure 7A-D due to the lower amount of evaporable water within these binders, because of the precipitation of voluminous ettringite in these binders, Figure 5E.

606 Figure 8 ranks the chloride ingress in various AAS binders as a function of slag chemistry
607 for each activator. In the case of NaOH-and Na_2CO_3-activated slags, the rate of chloride ingress
608 is correlated to the MgO content and the amounts of Mg-Al-OH LDH type phases formed.
609 However, in the case of Na_2CO_3-activated slags, it must be noted that the influence of
610 monocarbonate phases and the presence of minor quantities of CO_3^{2-} (aq.) species in the pore
611 solution, have not been considered to influence chloride binding. In the case of Na_2SiO_3- and
612 $Na_2O{\cdot}2SiO_2$-activated slags, M1 and M5 slags were found to have the slowest ingress of
613 chloride due to the formation of strätlingite and their chloride binding capability. For slags M6-
614 M14, the rate of chloride ingress is determined primarily by the amounts of Mg-Al-OH LDH
615 phase formed. In $Na_2O{\cdot}2SiO_2$-activated M11, M13 and M14 the precipitation of Ca-heulandite
616 and brucite influence the chloride binding capacity of the binder. In Na_2SO_4 activated slags,
617 the chloride binding capacities of monosulfate and ettringite have not been taken into account.
618 The rate of chloride ingress in low MgO containing slags (M1 and M5) is primarily influenced
619 by the presence of AFm, whereas in slags containing intermediate and high MgO (M6-M14),
620 chloride ingress is dependent on the amounts of C-(N-)A-S-H gel and Mg-Al-OH LDH formed.

621 It must be noted that the formation of strätlingite (or similar AFm phases) when low MgO
622 and high Al_2O_3 slags (particularly M1) are activated using Na_2SiO_3, $Na_2O{\cdot}2SiO_2$ and Na_2SO_4,
623 as predicted in this study and others [12,13], is not in agreement with the X-ray diffractograms
624 reported elsewhere including [18]. Instead, gismondine has been observed to form in these
625 slags [18] when activated with Na_2SiO_3, and monosulfoaluminate AFm when activated with
626 Na_2SO_4 [36]. This discrepancy can be attributed to the lack of reliable thermodynamic data for
627 gismondine in the thermodynamic database. Therefore, it could possibly be the case that the
628 extent of chloride binding and the ingress of chloride in Na_2SiO_3-, $Na_2O{\cdot}2SiO_2$- and Na_2SO_4-
629 activated M1 is overestimated, if these other potential phases have lower chloride binding
630 potential than strätlingite, but there are no available data to enable this to be assessed in detail.

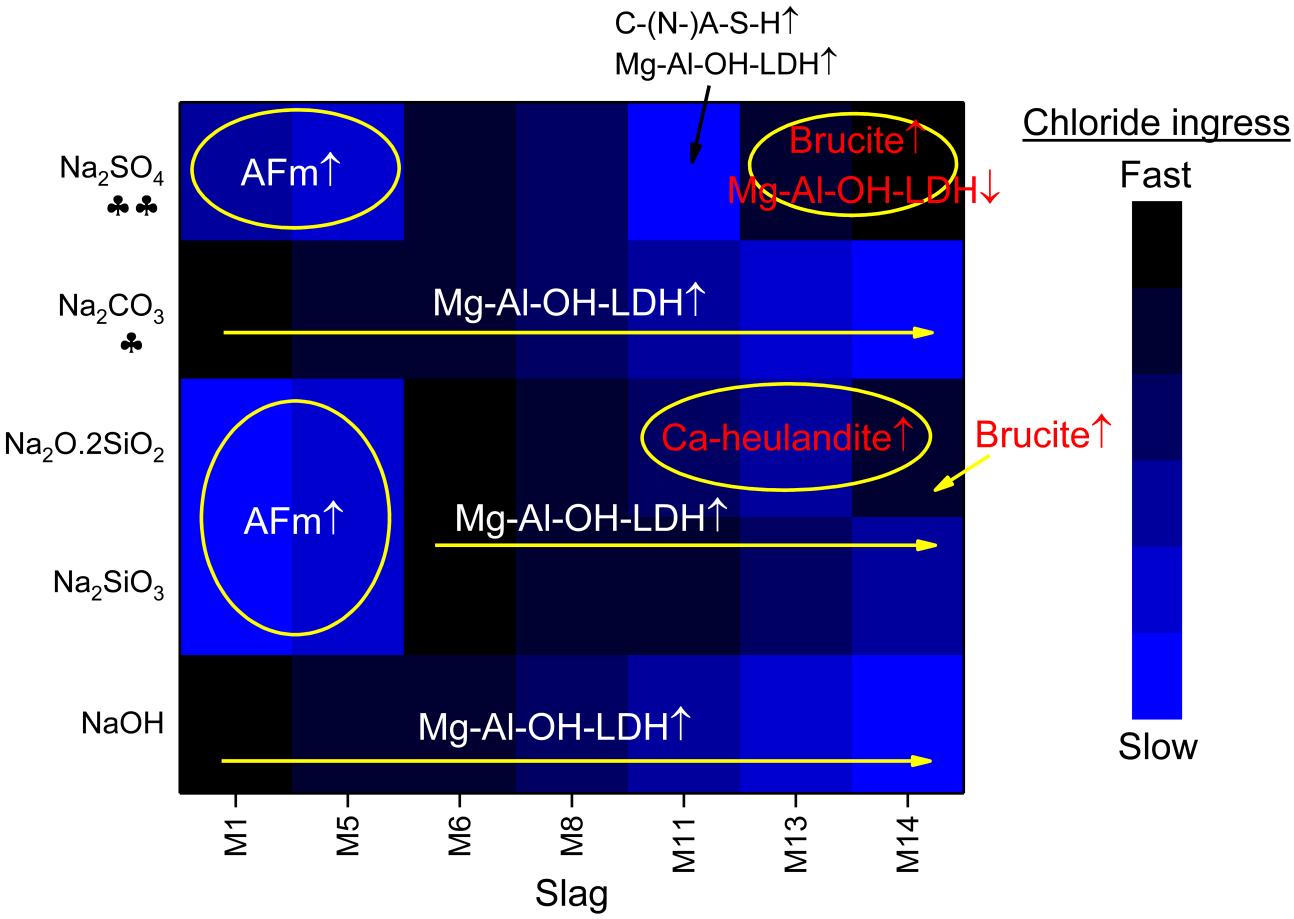

Figure 8: A schematic summarising the main parameters that influence chloride ingress in AAS concretes formulated using a wide range of GGBS and activators. Notes as marked on the graphic: ♣ In Na_2CO_3-activated GGBS, the influence of CO_3^{2-} ions in the pore solution and $C_4A\underline{c}H_{11}$ on chloride binding is not considered. ♣♣ In the case of Na_2SO_4-activated GGBS, chloride binding by ettringite or $C_4A\underline{s}H_{12}$ has not been taken into account.

4 Limitations and further development of the model

The model presented here is a significant step forward in linking AAS phase assemblage evolution and chloride binding to chloride transport. However, its extension is certainly possible, and several points have been identified where the existing body of data and literature require further development, to enable enrichment of the model and its use in the accurate prediction of service life for steel-reinforced structures based on AAS:

- Most importantly, the value of D_{Cl} in Eq. 7 was assumed to be the same for all AAS binders, and was based on the D_{nnsm} values observed experimentally [7,58]. However, in principle these values should vary for each of the slags and activators considered in

this study. Therefore, more experimental data are required to accurately separate the influence of chloride binding capacity and microstructure (pore structure – connectivity, tortuosity – and ITZ) on the $D_{app,Cl}$ (Eq. 7). Additionally, a better understanding of the influence of aggregates on chloride diffusion in AAS needs to be established and incorporated into the framework.

- Another major assumption made in this study was the scaling down of the theoretically calculated chloride binding isotherms to match the experimental binding isotherms for a particular AAS. The factor used for scaling down the theoretical chloride binding isotherms was extended to all slags and activators used. Most likely, this would be different for each of the slags, and therefore extensive experimental work needs to be carried out to draw empirical correlations between the activator used, the slag composition and the binding capacity of mortars/concretes based on AAS.

- Chloride binding isotherms for additional aluminate phases, particularly in the AFm and AFt families, need to be experimentally determined in simulated pore solutions representative of AAS, to ensure that the contributions of all phases identified in AAS towards chloride binding are considered. Extension of the isotherms to higher chloride concentrations would also be desirable.

- The phase assemblage database created in this study only considered slags with either 30 wt. % or 40 wt. % SiO_2, a constant SO_3 content of 2 wt. %, and fixed w/b ratios. However, a larger database for various SiO_2 and SO_3 contents and variable w/b ratio is needed to increase the accuracy in prediction of the chemistry of the binder. All parameters used in this study to quantify chloride binding and ingress relate to the solid and aqueous phase assemblages when the extent of slag reaction is 60 %. The extent of reaction could be extended from low values (representing early age) to 100 %, and its evolution while the concrete is in service integrated into the model.

- In the case of Na_2CO_3-activated slags, the influence of carbonate ions in the pore solution on the binding capacity of individual hydrate phases needs to be systematically understood.

- The alkalinity in this study was assumed to be constant with respect to space and time, and therefore the influence of carbonation and leaching were not considered. Experimental data are required to empirically draw a relationship between the chloride binding capacity and a reduction in pH of the pore solution due to carbonation and leaching.

- The chloride ingress profiles obtained using this modelling framework need to be validated by comparing with field data or laboratory data.

5 Conclusions, and further model development and implementation

This study provides the first ever modelling framework allowing the user to input the composition of the slag and the activator of interest to estimate the chemistry of the concrete cover, which can then be used to estimate the total chloride binding capacity of the binder within the concrete, and thus predict the time required for chloride to diffuse to the steel-concrete interface, as shown in Figure 9. This predictive modelling framework negates the need to use a mathematically 'incorrect' solution to Fick's second law, with a varying diffusion coefficient ($D_{app}\,(t)$) and the empirically derived age exponent. However, it would be necessary to point out that the model in its current state is conservative in nature (and only applicable for submerged structures) and several areas requiring more attention have been identified (Section 4) to enable enrichment of the framework.

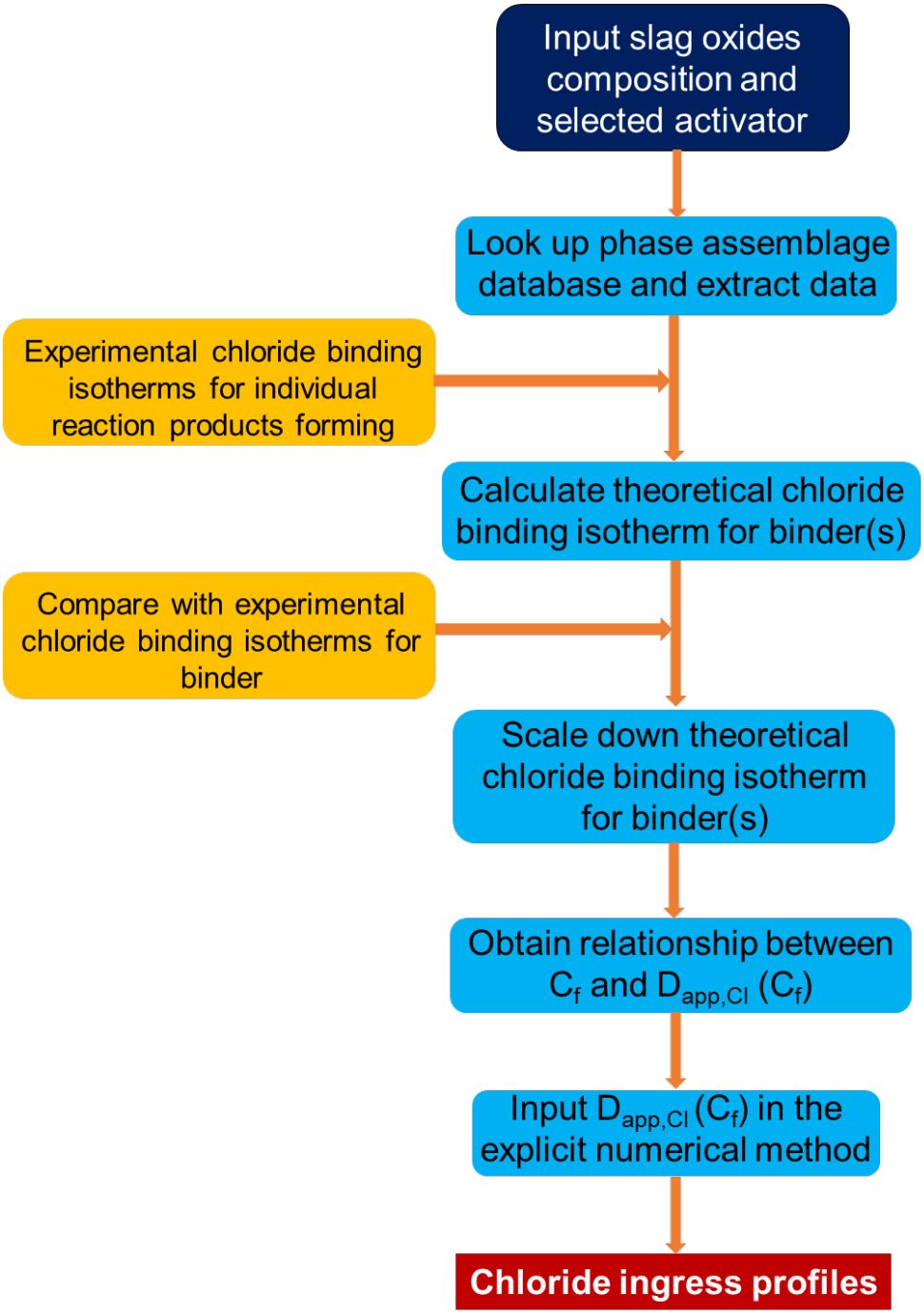

695

696 Figure 9: Schematic of the model developed in this study to calculate the ingress of chloride
697 in steel-reinforced concrete structures based out of AAS. Additional information regarding
698 chloride 'threshold' value needs to be experimentally determined to enable the modelled
699 chloride ingress profiles to be used to estimate the service life of steel-reinforced AAS
700 concretes.

701

6 Acknowledgements

The research leading to these results received funding from the European Research Council under the European Union's Seventh Framework Programme (FP/2007-2013) / ERC Grant Agreement #335928. The authors would like to thank Dr Xinyuan Ke for valuable discussions and for providing the chloride binding isotherms for individual hydrate phases from her PhD thesis. The contributions of D. Prentice were funded by the Engineering and Physical Sciences Research Council (EPSRC) UK in partnership with the National Nuclear Laboratory, through the iCASE scheme. The participation of S.A. Bernal in this study was partially funded by EPSRC through the ECF EP/R001642/1.

7 References

[1] K. Tuutti, Corrosion of steel in concrete, Swedish Cement and Concrete Research Institute, Stockholm, 1982.

[2] C. Arya, N.R. Buenfeld, J.B. Newman, Factors influencing chloride binding in concrete, Cem. Concr. Res. 20 (1990) 291–300.

[3] U.M. Angst, M.R. Geiker, A. Michel, C. Gehlen, H. Wong, O.B. Isgor, B. Elsener, C.M. Hansson, R. François, K. Hornbostel, R. Polder, M.C. Alonso, M. Sanchez, M.J. Correia, M. Criado, A. Sagüés, N. Buenfeld, The steel–concrete interface, Mater. Struct. 50 (2017) #143.

[4] U.M. Angst, M.R. Geiker, M.C. Alonso, R.B. Polder, O.B. Isgor, B. Elsener, H. Wong, A. Michel, K. Hornbostel, C. Gehlen, R. François, M. Sanchez, M. Criado, H. Sørensen, C.M. Hansson, R.G. Pillai, S. Mundra, J. Gulikers, M. Raupach, J. Pacheco, A. Sagüés, The effect of the steel-concrete interface on chloride-induced corrosion initiation in concrete: a critical review by RILEM TC 262-SCI, Mater. Struct. 52 (2019) #88.

[5] Q. Ma, S. V. Nanukuttan, P.A.M. Basheer, Y. Bai, C. Yang, Chloride transport and the resulting corrosion of steel bars in alkali activated slag concretes, Mater. Struct. 49 (2016) 3663–3677.

[6] I. Ismail, S.A. Bernal, J.L. Provis, R. San Nicolas, D.G. Brice, A.R. Kilcullen, S. Hamdan, J.S.J. Van Deventer, Influence of fly ash on the water and chloride permeability of alkali-activated slag mortars and concretes, Constr. Build. Mater. 48 (2013) 1187–1201.

[7] X. Ke, Improved durability and sustainability of alkali-activated slag cements. Ph.D. Thesis, The University of Sheffield, 2017.

[8] X. Ke, S.A. Bernal, J.L. Provis, Uptake of chloride and carbonate by Mg-Al and Ca-Al layered double hydroxides in simulated pore solutions of alkali-activated slag cement, Cem. Concr. Res. 100 (2017) 1–13.

738 [9] S. Mundra, S.A. Bernal, M. Criado, P. Hlaváček, G. Ebell, S. Reinemann, G.J.G. Gluth,
739 J.L. Provis, Steel corrosion in reinforced alkali - activated materials, RILEM Tech. Lett.
740 2 (2017) 33–39.

741 [10] U. Angst, B. Elsener, C.K. Larsen, Ø. Vennesland, Critical chloride content in reinforced
742 concrete - A review, Cem. Concr. Res. 39 (2009) 1122–1138.

743 [11] F. Winnefeld, M. Ben Haha, G. Le Saoût, M. Costoya, S.C. Ko, B. Lothenbach,
744 Influence of slag composition on the hydration of alkali-activated slags, J. Sustain. Cem.
745 Mater. 4 (2014) 85–100.

746 [12] R.J. Myers, S.A. Bernal, J.L. Provis, Phase diagrams for alkali-activated slag binders,
747 Cem. Concr. Res. 95 (2017) 30–38.

748 [13] R.J. Myers, B. Lothenbach, S.A. Bernal, J.L. Provis, Thermodynamic modelling of
749 alkali-activated slag cements, Appl. Geochemistry. 61 (2015) 233–247.

750 [14] R.J. Myers, S.A. Bernal, J.L. Provis, A thermodynamic model for C-(N-)A-S-H gel:
751 CNASH_ss. Derivation and validation, Cem. Concr. Res. 66 (2014) 27–47.

752 [15] S.A. Bernal, V. Rose, J.L. Provis, The fate of iron in blast furnace slag particles during
753 alkali-activation, Mater. Chem. Phys. 146 (2014) 1–5.

754 [16] X. Ke, S.A. Bernal, J.L. Provis, Controlling the reaction kinetics of sodium carbonate-
755 activated slag cements using calcined layered double hydroxides, Cem. Concr. Res. 81
756 (2016) 24–37.

757 [17] M. Ben Haha, G. Le Saoût, F. Winnefeld, B. Lothenbach, Influence of activator type on
758 hydration kinetics, hydrate assemblage and microstructural development of alkali
759 activated blast-furnace slags, Cem. Concr. Res. 41 (2011) 301–310.

760 [18] S.A. Bernal, R. San Nicolas, R.J. Myers, R. Mejía de Gutiérrez, F. Puertas, J.S.J. Van
761 Deventer, J.L. Provis, MgO content of slag controls phase evolution and structural
762 changes induced by accelerated carbonation in alkali-activated binders, Cem. Concr.
763 Res. 57 (2014) 33–43.

764 [19] D.A. Kulik, T. Wagner, S. V. Dmytrieva, G. Kosakowski, F.F. Hingerl, K. V.
765 Chudnenko, U.R. Berner, GEM-Selektor geochemical modeling package: Revised
766 algorithm and GEMS3K numerical kernel for coupled simulation codes, Comput.
767 Geosci. 17 (2013) 1–24.

768 [20] T. Wagner, D.A. Kulik, F.F. Hingerl, S. V Dmytrieva, GEM-Selektor geochemical
769 modeling package: TSolMod library and data interface for multicomponent phase
770 models, Can. Mineral. 50 (2012) 1173–1195.

771 [21] CEMDATA14, (2017). https://www.empa.ch/web/s308/cemdata (accessed November
772 23, 2017).

773 [22] H.C. Helgeson, D.H. Kirkham, G.C. Flowers, Theoretical prediction of the
774 thermodynamic behavior of aqueous electrolytes by high pressures and temperatures.
775 IV, Calculation of activity coefficients, osmotic coefficients, and apparent molal &
776 standard relative partial molal properties to 600°C & 5kB, Am. J. Sci. 281 (1981) 1249–

777 1516.

778 [23] B. Martin-Pérez, H. Zibara, R.D. Hooton, M.D.A. Thomas, A study of the effect of
779 chloride binding on service life predictions, Cem. Concr. Res. 30 (2000) 1215–1223.

780 [24] G. Sergi, S.W. Yu, C.L. Page, Diffusion of chloride and hydroxyl ions in cementitious
781 materials exposed to a saline environment, Mag. Concr. Res. 44 (1992) 63–69.

782 [25] L. Tang, L.O. Nilsson, Chloride binding capacity and binding isotherms of OPC pastes
783 and mortars, Cem. Concr. Res. 23 (1993) 247–253.

784 [26] H. Zibara, Binding of external chloride by cement pastes. Ph.D. Thesis, University of
785 Toronto, Canada, 2001.

786 [27] NT Build 492, Concrete, mortar and cement-based repair materials: Chloride migration
787 coefficient from non-steady-state migration experiments, Nordtest Methods, 1999.

788 [28] L. Tang, Chloride transport in concrete - Measurement and prediction. Ph.D. Thesis,
789 Chalmers University of Technology, 1996.

790 [29] European Union - Brite EuRam III, DuraCrete - General guidelines for durability design
791 and redesign. Probabilistic performance based durability design of concrete structures,
792 2000.

793 [30] International Federation of Structural Concrete (fib), fib Model Code for Service Life
794 Design, 2006.

795 [31] P. Spiesz, M.M. Ballari, H.J.H. Brouwers, RCM: A new model accounting for the non-
796 linear chloride binding isotherm and the non-equilibrium conditions between the free-
797 and bound-chloride concentrations, Constr. Build. Mater. 27 (2012) 293–304.

798 [32] Q. Yuan, Fundamental studies on test methods for the transport of chloride ions in
799 cementitious materials. Ph.D. Thesis, University of Ghent, 2009.

800 [33] E. Samson, J. Marchand, K.A. Snyder, Calculation of ionic diffusion coefficients on the
801 basis of migration test results, Mater. Struct. 36 (2003) 156–165.

802 [34] J. Zheng, H.S. Wong, N.R. Buenfeld, Assessing the influence of ITZ on the steady-state
803 chloride diffusivity of concrete using a numerical model, Cem. Concr. Res. 39 (2009)
804 805–813.

805 [35] M. Ben Haha, B. Lothenbach, G. Le Saoût, F. Winnefeld, Influence of slag chemistry
806 on the hydration of alkali-activated blast-furnace slag - Part II: Effect of Al_2O_3, Cem.
807 Concr. Res. 42 (2012) 74–83.

808 [36] S.A. Bernal, X. Ke, J.L. Provis, Activation of slags using near-neutral salts: The
809 importance of slag chemistry, in: 14th Int. Congr. Chem. Cem. (ICCC 2015), Beijing,
810 2015.

811 [37] Y. Elakneswaran, T. Nawa, K. Kurumisawa, Electrokinetic potential of hydrated cement
812 in relation to adsorption of chlorides, Cem. Concr. Res. 39 (2009) 340–344.

813 [38] I. Galan, F.P. Glasser, Chloride in cement, Adv. Cem. Res. 27 (2015) 63–97.

814 [39] H. Hirao, K. Yamada, H. Takahashi, H. Zibara, Chloride binding of cement estimated
815 by binding isotherms of hydrates, J. Adv. Concr. Technol. 3 (2005) 77–84.

816 [40] J. Crank, The Mathematics of Diffusion, 2nd ed., Oxford University Press, 1975.

817 [41] V.G. Papadakis, M.N. Fardis, C.G. Vayenas, Physiochemical processes and
818 mathematical modeling of concrete chlorination, Chem. Eng. Sci. 51 (1996) 505–513.

819 [42] I.G. Richardson, G.W. Groves, Microstructure and microanalysis of hardened cement
820 pastes involving ground granulated blast-furnace slag, J. Mater. Sci. 27 (1992) 6204–
821 6212.

822 [43] F. Bonk, J. Schneider, M.A. Cincotto, H. Panepucci, Characterization by multinuclear
823 high-resolution NMR of hydration products in activated blast-furnace slag pastes, J. Am.
824 Ceram. Soc. 86 (2003) 1712–1719.

825 [44] M. Ben Haha, B. Lothenbach, G. Le Saoût, F. Winnefeld, Influence of slag chemistry
826 on the hydration of alkali-activated blast-furnace slag - Part I: Effect of MgO, Cem.
827 Concr. Res. 41 (2011) 955–963.

828 [45] M.U. Okoronkwo, F.P. Glasser, Stability of strätlingite in the CASH system, Mater.
829 Struct. 49 (2016) 4305–4318.

830 [46] J.L. Provis, S.A. Bernal, Geopolymers and related alkali-activated materials, Annu. Rev.
831 Mater. Res. 44 (2014) 299–327.

832 [47] R.J. Myers, S.A. Bernal, J.D. Gehman, J.S.J. Van Deventer, J.L. Provis, The role of Al
833 in cross-linking of alkali-activated slag cements, J. Am. Ceram. Soc. 98 (2015) 996–
834 1004.

835 [48] F. Puertas, M. Palacios, H. Manzano, J.S. Dolado, A. Rico, J. Rodríguez, A model for
836 the CASH gel formed in alkali-activated slag cements, J. Eur. Ceram. Soc. 31 (2011)
837 2043–2056.

838 [49] I.G. Richardson, A.R. Brough, G.W. Groves, C.M. Dobson, The characterization of
839 hardened alkali-activated blast-furnace slag pastes and the nature of the calcium silicate
840 hydrate (C-S-H) phase, Cem. Concr. Res. 24 (1994) 813–829.

841 [50] A.M. Rashad, Y. Bai, P.A.M. Basheer, N.B. Milestone, N.C. Collier, Hydration and
842 properties of sodium sulfate activated slag, Cem. Concr. Compos. 37 (2013) 20–29.

843 [51] N. Mobasher, S.A. Bernal, J.L. Provis, Structural evolution of an alkali sulfate activated
844 slag cement, J. Nucl. Mater. 468 (2016) 97–104.

845 [52] N. Mobasher, S.A. Bernal, O.H. Hussain, D.C. Apperley, H. Kinoshita, J.L. Provis,
846 Characterisation of $Ba(OH)_2$-Na_2SO_4-blast furnace slag cement-like composites for the
847 immobilisation of sulfate bearing nuclear wastes, Cem. Concr. Res. 66 (2014) 64–74.

848 [53] S.A. Bernal, Advances in near-neutral salts activation of blast furnace slags, RILEM
849 Tech. Lett. 1 (2016) 39–44.

850 [54] G.K. Glass, N.R. Buenfeld, The influence of chloride binding on the chloride induced

851 corrosion risk in reinforced concrete, Corros. Sci. 42 (2000) 329–344.

852 [55] L. Tang, J. Gulikers, On the mathematics of time-dependent apparent chloride diffusion
853 coefficient in concrete, Cem. Concr. Res. 37 (2007) 589–595.

854 [56] K.Y. Foo, B.H. Hameed, Insights into the modeling of adsorption isotherm systems,
855 Chem. Eng. J. 156 (2010) 2–10.

856 [57] F. Haghseresht, G.Q. Lu, Adsorption characteristics of phenolic compounds onto coal-
857 reject-derived adsorbents, Energy Fuels. 12 (1998) 1100–1107.

858 [58] X. Ke, S.A. Bernal, O.H. Hussein, J.L. Provis, Chloride binding and mobility in sodium
859 carbonate-activated slag pastes and mortars, Mater. Struct. 50 (2017) 252.

860 [59] A. Mesbah, J.P. Rapin, M. Franąois, C. Cau-Dit-Coumes, F. Frizon, F. Leroux, G.
861 Renaudin, Crystal structures and phase transition of cementitious Bi-anionic AFm-(Cl^-,
862 CO_3^{2-}) compounds, J. Am. Ceram. Soc. 94 (2011) 261–268.

863 [60] A. Mesbah, C. Cau-Dit-Coumes, F. Frizon, F. Leroux, J. Ravaux, G. Renaudin, A new
864 investigation of the Cl^--CO_3^{2-} substitution in AFm phases, J. Am. Ceram. Soc. 94 (2011)
865 1901–1910.

866 [61] L. Châtelet, J.Y. Bottero, J. Yvon, A. Bouchelaghem, Competition between monovalent
867 and divalent anions for calcined and uncalcined hydrotalcite: anion exchange and
868 adsorption sites, Colloids Surfaces A Physicochem. Eng. Asp. 111 (1996) 167–175.

869 [62] U.A. Birnin-Yuari, F.P. Glasser, Friedel's salt, $Ca_2Al(OH)_6(Cl,OH).2H_2O$: Its solid
870 solutions and their role in chloride binding, Cem. Concr. Res. 28 (1998) 1713–1723.

871

872